Structured Light 3D Imaging Instrument for Biological Tissues With Potential Application in Telemedicine

Yan Hu, Zhongwei Liang, Kehui Wang, Kun Gui, Jin Zhang, Qian Chen, and Chao Zuo, *Senior Member, IEEE*

***Abstract*— Pathology telemedicine helps to receive technical guidance from sophisticated experts through media, which assists cancer consultation in hospitals far away. This article proposes a 3D imaging and interactive cutting lines projection system comprising a digital projector and three color cameras. A 3D imaging and the function of projecting interactive markers on specified parts of the sample surface are realized, facilitating remote experts' pseudo-painting for guiding biological operations. Within each subsystem that works using one camera and the projector, sinusoidal patterns with stripes perpendicular to the baseline are designed to ensure high signal-to-noise ratio 3D results. A phase mapping-based method for projector calibration is proposed by finding the diagonal center of the white squares on the checkboard, avoiding the effect of perspective distortion on the center positioning of circular markers. A point cloud denoising strategy, including phase consistency check and jump region identification, is proposed, allowing the system to perceive detailed morphology without discrete points. Each 3D reconstruction time is less than 3 s, including data acquisition and processing. The accuracy evaluation experiments on the standard plane and sphere show that our system achieves 3D results with a repeatability error of less than 10 μm at a field of view of 6 × 10 cm, which meets the imaging requirements for pathology telemedicine support.**

Manuscript received 20 October 2023; accepted 27 October 2023. Date of publication 13 November 2023; date of current version 22 December 2023. This work was supported in part by the National Natural Science Foundation of China under Grant 62005121, Grant 62075096, and Grant U21B2033; in part by the Leading Technology of Jiangsu Basic Research Plan under Grant BK20192003; in part by the "333 Engineering" Research Project of Jiangsu Province under Grant BRA2016407; in part by the Jiangsu Provincial "One belt and One Road" Innovation Cooperation Project under Grant BZ2020007; in part by the Fundamental Research Funds for the Central Universities under Grant 30921011208, Grant 30919011222, and Grant 30920032101; in part by the China Postdoctoral Science Foundation under Grant 2022M721619; and in part by the Open Research Fund of Jiangsu Key Laboratory of Spectral Imaging and Intelligent Sense under Grant JSGP202103. The Associate Editor coordinating the review process was Dr. Pranab K. Dutta. *(Yan Hu and Zhongwei Liang contributed equally to this work.) (Corresponding author: Chao Zuo.)*

Yan Hu, Zhongwei Liang, and Chao Zuo are with the Jiangsu Key Laboratory of Spectral Imaging and Intelligent Sense and the Smart Computational Imaging Laboratory (SCILab), Nanjing University of Science and Technology, Nanjing, Jiangsu 210094, China (e-mail: hu_yan@njust.edu.cn; liangzw@njust.edu.cn; zuochao@njust.edu.cn).

Kehui Wang and Kun Gui are with Konfoong Biotech International Company Ltd., Ningbo, Zhejiang 315499, China (e-mail: Kehui.wang@kfbio.cn; kun.gui@kfbio.cn).

Jin Zhang is with the Ningbo Diagnostic Pathology Center, Ningbo, Zhejiang 315021, China (e-mail: 593913653@qq.com).

Qian Chen is with the Jiangsu Key Laboratory of Spectral Imaging and Intelligent Sense, Nanjing University of Science and Technology, Nanjing, Jiangsu 210094, China (e-mail: chenqian@njust.edu.cn).

Digital Object Identifier 10.1109/TIM.2023.3331396

***Index Terms*— 3D telemedicine, fringe projection, marker reverse projection, pathology, structured light.**

I. Introduction

THANKS to the invention of various sensors, human beings' ability to access information has continuously improved. Information that used to be accessible through instantaneous sounds in our ears or fleeting scenes in our eyes can now be stored in higher dimensional multimedia. People can share video, images, sound, and other data to any corner of the world in real time. Detail-rich pathology images can aid in the early diagnosis of cancer [1], [2], and pathology telemedicine utilizes modern communication equipment to share remote medical technology and resources [3], [4]. However, most traditional telemedicine data are based on 2-D image or video formats. They are fast in transmission but have such a low dimension of information [5], [6]. Suppose the dimension of the transmitted information is increased, for example, by using 3D imaging and display for assistance. In that case, remote experts can visualize live scenes as if they were right there, and this is a quantum leap in improving telemedicine's communication efficiency and capability.

The emergence of fast 3D sensing techniques [7], [8], [9], [10], [11], [12], [13], [14] provides technical approaches for recording real-world scenes rapidly. Based on 2-D images, these techniques are widely used in man–machine interactive amusement [15]. However, these 3D imaging techniques can only achieve a measurement accuracy that roughly recognizes the posture of the human body. Since biological tissues are relatively soft, moving them during measurement can deform them. Therefore, a complete range of measurements can only be achieved by synthesizing measured results from different perspectives, which decreases measurement efficiency. Laser line scanning can deal with 3D measurements of complex surface morphology [16], but its characteristics, such as the need for manual handheld and operation back and forth, are not conducive to nonprofessional personnel in the medical environment. Phase-shifting-based fringe projection profilometry (PS-FPP) has the advantages of the full field of view, high accuracy, fast speed, and noncontact [17], [18], [19], [20], offering a technical reference for 3D imaging of biological tissues.

The systems with a multiview structure may be the solution to the integrated 3D imaging of complex shapes. However, most systems essentially contain two cameras with symmetrical left–right structures [21], [22], [23], [24], which cannot fully measure 3D morphology in the direction perpendicular to the camera's optical axis. It is not easy to apply measurement systems with too many views when large working distances are required because a more extended baseline between each camera and the projector is necessary to ensure measurement accuracy, which needs a larger system volume. Cheng et al. [25] proposed an MFPP system comprising three Scheimpflug projectors and a telecentric lens to realize 3D imaging in optical inspection. Although the Scheimpflug principle enhances the measurable depth of field, it is still not suitable for measuring the shape of the size of pathological tissue samples. Wang et al. [26] proposed a four-view fringe projection 3D microscopy system and achieved vertical stitching of samples at different depths. However, the color information are missing, and the working distance varies within only several millimeters.

A color camera can provide color texture for a calibrated 3D measurement system [27]. However, smooth surfaces are needed; otherwise, full-range color information are inaccessible. Scholars have also proposed using the three channels of color cameras for structured light 3D measurement [28], [29], [30], [31], [32]. On the one hand, the color information captured by the three color channels can restore the object's color texture, and on the other hand, the three coded patterns for phase shifting can be obtained through the three channels of the color image by taking one photograph.

Considering the following factors: the requirement for color integrity, the compact volume of the structure, and the hardware cost, we design a system that contains three cameras for multiimaging views. However, arranging the camera positions and orientation and designing optimal encoded patterns for each 3D measurement subsystem is necessary to achieve the best 3D reconstruction accuracy. So, in this article, we present a low-cost structured light 3D measuring instrument for telemedicine.

In the face of some unique challenges that are difficult to address with traditional methods in telemedicine, we put forward corresponding solutions. For accurate projector calibration, we propose using the diagonal center of the white squares on the checkboard as feature points, eliminating the bias in feature point extraction due to perspective distortion. Based on the disparity maximization criterion, we designed coded fringe patterns with optimized orientations for the single projector and a new computational model based on the equiphase plane is proposed to retrieve 3D data. A fusion method combining 3D data and ring LED illuminated 2-D color is proposed for better color integrity of pathological samples. A denoising strategy based on their unique characteristics is also proposed to filter out the invalid points caused by object shadows, occlusions, high reflections, and truncated areas. Last is the inverse projection function that projects the marker pattern drawn on the target photograph by the expert onto the sample surface to guide the operator to cut the sample. By digitizing pathological issues in the form of color 3D data, a new way for telemedicine guidance is realized.

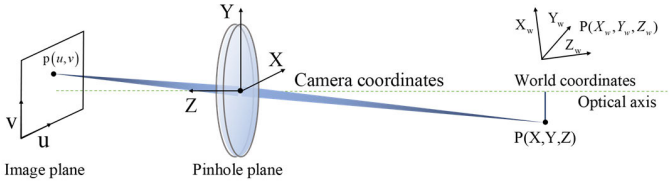

Fig. 1. Perspective model and imaging process from the object to the image sensor of a pinhole camera.

II. Theory

This section introduces the basic definition of imaging models and methods related to our instrument, mainly including the perspective mapping model used to establish the geometric model of projection and imaging optical paths, constraints between equiphase plane and camera pixel lines used to describe how to solve the 3D location by using camera and projection model, and phase retrieval from phase-shifting fringe images to obtain quantitative information about the sample's morphology.

A. Perspective Mapping Model

Referring to Fig. 1, suppose a point $\mathrm{P}(X_w, Y_w, Z_w)$ in the world coordinate is imaged on the image plane, denoted by a point $\mathrm{p}(u, v)$. The world and camera coordinate systems are related by an external parameter matrix $\mathbf{T}$, consisting of three rotation vectors $\mathbf{r}_{1\text{-}3}$ and a translation vector $\mathbf{t}$. Therefore, the transformation from the world coordinates to the image plane can be expressed as follows:

$$Z\begin{bmatrix} u \\ v \\ 1 \end{bmatrix} = \underbrace{\begin{bmatrix} f_x & 0 & u_0 \\ 0 & f_y & v_0 \\ 0 & 0 & 1 \end{bmatrix}}_{\mathbf{A}} \underbrace{\begin{bmatrix} r_{11} & r_{12} & r_{13} & t_x \\ r_{21} & r_{22} & r_{23} & t_y \\ r_{31} & r_{32} & r_{33} & t_z \end{bmatrix}}_{\mathbf{T}} \begin{bmatrix} X_w \\ Y_w \\ Z_w \\ 1 \end{bmatrix}. \tag{1}$$

Here, Z is the z-axis coordinate of the object in the camera coordinate system, and $\mathbf{A}$ is the intrinsic matrix that connects the camera coordinates to the image ones. It can be obtained by simple linear transformation as follows:

$$\begin{cases} u = f_x \cdot \dfrac{X}{Z} + u_0 \\ v = f_y \cdot \dfrac{Y}{Z} + v_0. \end{cases} \tag{2}$$

Here, (u_0, v_0) is the image coordinate of the optical center. (f_x, f_y) is the horizontal and vertical focal length. We use subscripts c and p to represent parameters about the camera and projector, respectively.

B. Constraints on the Intersection of the Equiphase Plane With Camera Pixel Lines

In order to solve the world coordinates of the object, we need to provide another constraint equation in addition to

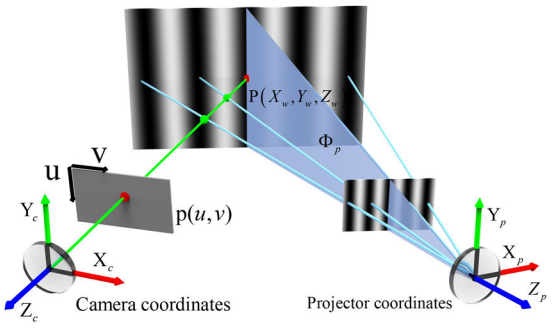

Fig. 2. 3D coordinates constraints based on the intersection of the equiphase plane and the camera pixel line.

the two constraints obtained from (2). A feasible solution is to give another constraint on the intersection of an equiphase plane of the projector with the pixel lines of the camera. As shown in Fig. 2, the pixel line from the camera sensor plane and the equiphase plane Φ_p from the projector pattern source plane intersect at the surface of the target in physical space as point $P(X_w, Y_w, Z_w)$. Therefore, the world coordinate (X_w, Y_w, Z_w) can be calculated by combining the equiphase plane and pixel line equations.

C. Phase Retrieval From Phase-Shifting Images

In order to obtain the phase values, we need phase shifting and unwrapping based on the structured light fringe patterns. Vertical sinusoidal patterns with several periods and phase shifts are projected in sequence. Based on the calibration parameters and the calculated phase, we can retrieve the 3D shape of the object's surface. The phase-shifting algorithm can obtain the quantitative fringe distortion. The image intensity with a phase shift $2\pi/N$ of the sinusoidal fringe can be written as follows:

$$I_n(u, v) = A(u, v) + B(u, v)\cos\left[\Phi(u, v) - 2\pi n/N\right] \quad (3)$$

where n is the number of image index, and N is the number of images. A is the background. B is the modulation. Φ is the absolute unwrapped phase. The wrapped phase ϕ of Φ can be obtained by

$$\phi(u, v) = -\arctan\left[\frac{\sum_{n=1}^{N} I_n(u, v)\sin(2\pi n/N)}{\sum_{n=1}^{N} I_n(u, v)\cos(2\pi n/N)}\right]. \quad (4)$$

The phase value calculated by (4) is in the range of $(0, 2\pi]$. It is necessary to compensate the fringe orders to get a continuous phase map. The multifrequency unwrapping algorithm [33] uses fringe patterns that have different frequencies, based on which the unwrapped phase Φ_i is obtained by adding a certain order k that times 2π to the wrapped phase ϕ_i

$$\Phi_i(u, v) = \phi_i(u, v) + 2\pi k_i(u, v) \quad (5)$$

where k_i is the fringe order, which indicates the location of every fringe stripe. The detailed information of the phase-shifting patterns we used is presented in Table I.

TABLE I
DETAIL INFORMATION OF THE PHASE-SHIFTING PATTERNS

Items	Values		
i (fringe set)	1	2	3
N_i (phase-shifting number)	4	4	8
P_i (fringe period in pixels)	1140	200	36
Fringe frequency	1	5.7	31.67

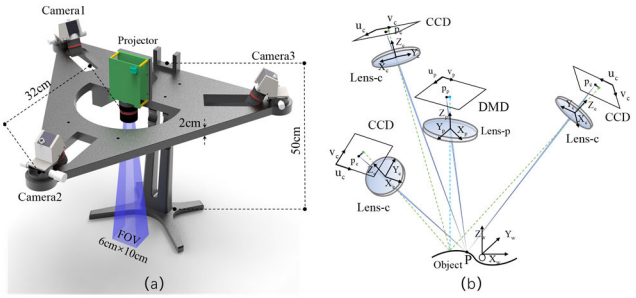

Fig. 3. System architecture and coordinates systems of the optical components. (a) 3D modeling of the triple-view system, containing a projector and three cameras with orientations toward the center of the field of view. (b) Geometrical relationship of the optical axis, target surface, and coordinate systems.

III. System Design and Methodology

A. System Architecture

A triple-view system is built as shown in Fig. 3(a). The main structure of the system is a triangular platform made of photosensitive resin material with a thickness of 2 cm, on which we have a digital projector (DLP 4500, resolution: 912 × 1140) and three color cameras (ImagingSource DFK 33UX183, resolution: 3648 × 5472) attached with a Computar M3Z1228C-MP lens. The overall height is 50 cm, and a field of view of 10 × 6 cm can be realized. The exposure of the cameras and projector is synchronized through trigger signals. The coordinate relationships between various views of the system are shown in Fig. 3(b).

The projector is fixed in the center of the platform, which can be adjusted up and down and then locked in an appropriate place. Each camera is locked to the platform by a Cardan joint and is 32 cm away from the center projector, which ensures that samples can be observed from multiple views. The center and three corners of the platform are windowed appropriately to allow light to pass through freely. The platform can be fixed by towing or linked with the bracket through a lifting platform (our system uses), which can also be adjusted to different heights to change working distance.

To implement the 3D measurements, we first designed the coding pattern using MATLAB and then loaded it into the projector via the programming interface. Simultaneous exposure between the cameras and the projector is required, which is realized by trigger signals from the projector. The computer, then, receives a series of real-time images from each camera, in turn, via high-speed serial cables. In the first phase, we develop and validate calibration and reconstruction algorithms on the MATLAB platform and subsequent data analysis and comparison. The final application software development

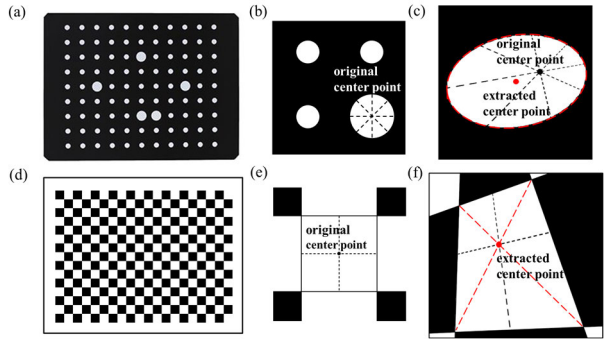

Fig. 4. Effect of perspective distortion on the extraction of feature points. (a) Regular board with circular markers. (b) Details of the circular markers without distortion. (c) Errors of extraction occur due to distortion. (d) Regular checkerboard. (e) Details of white squares without distortion. (f) No errors of extraction occur due to distortion.

and implementation is done on the Visual Studio platform using the C++ language.

The user places the sample on the platform and performs the measurement function. The acquisition rate is 60 frames/s, and each view requires the camera to capture 16 images. It takes less than 1 s to complete data acquisition for all three views. Due to the high image resolution, the algorithm needs to be accelerated by combining techniques such as multithreading and parallel acceleration, and the reconstruction of the complete 3D data can be completed in 1–2 s (depending on the computer's computing power).

B. Projector Calibration

Refer to Fig. 3(b), we define the pinhole projection model of the projector as follows:

$$Z_p\begin{bmatrix} u_p \\ v_p \\ 1 \end{bmatrix} = \underbrace{\begin{bmatrix} f_{xp} & 0 & u_{p0} \\ 0 & f_{yp} & v_{p0} \\ 0 & 0 & 1 \end{bmatrix}}_{\mathbf{A_p}} \times \underbrace{\begin{bmatrix} r_{p11} & r_{p12} & r_{p13} & t_{px} \\ r_{p21} & r_{p22} & r_{p23} & t_{py} \\ r_{p31} & r_{p32} & r_{p33} & t_{pz} \end{bmatrix}}_{\mathbf{T_p}} \begin{bmatrix} X_w \\ Y_w \\ Z_w \\ 1 \end{bmatrix}. \quad (6)$$

The projector calibration usually uses circular markers to provide control points. A commonly used pattern is shown in Fig. 4(a). Like the camera calibration, we need to obtain the world and image coordinates of feature points. The projector requires phase values to help and locate the coordinates of the feature points on the digital micromirror devices (DMDs) plane. The relationship between the pixel coordinates (u_p, v_p) and the phase (Φ_x, Φ_y) is

$$\begin{cases} u_p = \dfrac{\Phi_x}{2\pi \mathrm{N}_x}\omega_x \\ v_p = \dfrac{\Phi_y}{2\pi \mathrm{N}_y}\omega_y. \end{cases} \quad (7)$$

Here, $(\mathrm{N}_x, \mathrm{N}_y)$ is the period number of the projected sinusoidal pattern, and (ω_x, ω_y) is the number of pixels each period occupies. The phase-shifting algorithm can obtain the phase value (Φ_x, Φ_y) at the feature point in two directions.

As we can see from Fig. 4(a)–(c), errors of extraction occur due to the perspective distortion. We propose using the diagonal center of the white squares on the checkboard as feature points. They can be determined by searching the diagonal intersection of the white squares. In this way, the effect of perspective distortion on the center positioning of circular markers is avoided, as shown in Fig. 4(d)–(f).

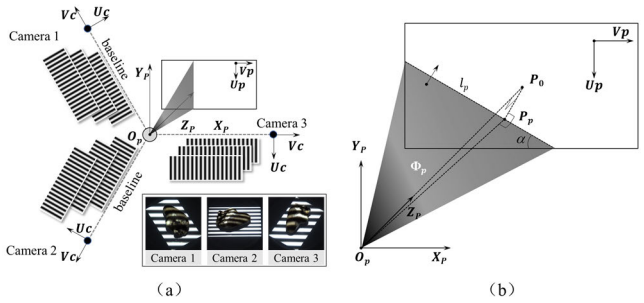

Fig. 5. Tilted fringe patterns design and geometrical diagram of the equiphase plane. (a) Schematic of the orientation adjustment of the fringe direction at each subview. (b) Schematic illustrating the reconstruction of 3D coordinates from tilted fringes.

C. Coded Fringe Patterns With Maximum Phase Disparity

In structured light 3D measurement, to meet the needs of different measurement scenarios, structured light is designed into a pattern different from the traditional single-direction form [34], [35], [36]. In this article, to ensure high signal-to-noise ratio 3D results, the phase gradient direction of the coded sinusoidal patterns must follow the baseline direction between the camera and the projector. Based on the layout of the cameras and the projector in our system, the fringe direction of each view is adjusted, as shown in Fig. 5(a). In this way, the error transfer coefficient from phase-to-3D result is minimized in all subsystems, assuring high-accuracy 3D reconstructions.

Since the system has only one projector, the direction of its projected fringe needs to be adjusted according to each camera. Let us take camera 2 in Fig. 5 as an example. Assume that (k_a, k_b, k_c) is the normal vector of equiphase plane Φ_p on which point $\mathrm{P}_p(X_p, Y_p, Z_p)$ locates. Then, we have

$$k_a X_p + k_b Y_p + k_c Z_p = 0. \quad (8)$$

The normal vector of equiphase plane Φ_p can be obtained through the cross-product of two orthogonal vectors in Φ_p. Here, we take $\mathbf{O_pP_p}$ and $\mathbf{l}_p$. $\mathbf{l}_p$ is the direction vector of line l_p in the DMD plane, which is also the fringe direction, so we have

$$(k_a, k_b, k_c) = \mathbf{O_pP_p} \times \mathbf{l}_p. \quad (9)$$

Suppose the angle between the fringe direction $\mathbf{l}_p$ and the horizontal direction $\boldsymbol{X}_P$ is α; then, we have

$$\begin{cases} \mathbf{l_p} = (\sin\alpha, \cos\alpha, 0) \\ \mathbf{O_pP_p} = \mathbf{O_pP_0} + \mathbf{P_0P_p}. \end{cases} \quad (10)$$

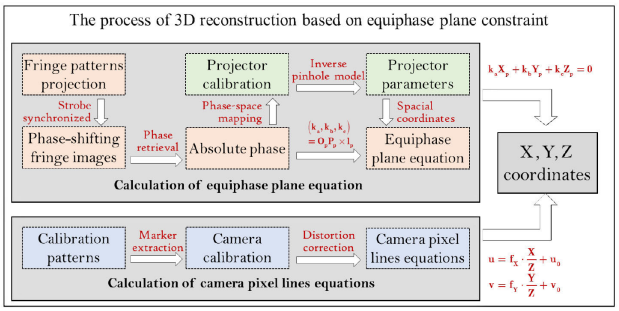

Fig. 6. Flowchart of the 3D reconstruction process for a single view. The camera provides 2-D coordinates, and the projector provides another phase-determined plane equation. The final 3D coordinates are calculated by jointly solving the equations.

Here, $\mathbf{O_pP_0}$ and $\mathbf{P_0P_p}$ can be obtained as follows:

$$\begin{cases} \mathbf{O_pP_0} = (0, 0, f_p) \\ \mathbf{P_0P_p} = (\cos\alpha, \sin\alpha, 0) \cdot (\varphi_p - \varphi_0) \cdot l_\varphi. \end{cases} \tag{11}$$

Here, f_p is the focal length of the projector lens, φ_p and φ_0 are the phase values at the point P_p and the principal point P_0, respectively. l_φ is the distance occupied by the unit phase along the phase gradient direction. The relationship between $\mathrm{P}_c(X_c, Y_c, Z_c)$ in the camera coordinate system and $\mathrm{P}_p(X_p, Y_p, Z_p)$ in the projector coordinate system can be expressed as follows:

$$\begin{bmatrix} X \\ Y \\ Z \end{bmatrix} = \mathbf{T_p^+} \cdot \begin{bmatrix} X_p \\ Y_p \\ Z_p \\ 1 \end{bmatrix} = \mathbf{T_c^+} \cdot \begin{bmatrix} X_c \\ Y_c \\ Z_c \\ 1 \end{bmatrix} \tag{12}$$

where "+" means pseudo-inverse of a matrix. Combining (8), we have another constraint equation

$$\underbrace{\begin{bmatrix} k_a & k_b & k_c \end{bmatrix} \cdot \mathbf{T_P} \cdot \mathbf{T_c^+}}_{\mathbf{M}} \begin{bmatrix} X_c \\ Y_c \\ Z_c \\ 1 \end{bmatrix} = 0. \tag{13}$$

Because (k_a, k_b, k_c), $\mathbf{T_P}$ and $\mathbf{T_C^+}$ can be determined in advance to be integrated into a single matrix $\mathbf{M}$

$$\mathbf{M} = \begin{bmatrix} k_a & k_b & k_c \end{bmatrix} \cdot \mathbf{T_P} \cdot \mathbf{T_c^+}. \tag{14}$$

By calculating the camera imaging model (1) and (13), we can directly calculate the coordinates of the object point in the following matrix-based form:

$$\begin{cases} X_c = (u_c - u_{c0}) Z_c / f_{xc} \\ Y_c = (v_c - v_{c0}) Z_c / f_{yc} \\ Z_c \\ \quad = \dfrac{-\mathbf{M}(1,4)}{(u_c - u_{c0})/f_{xc} \cdot \mathbf{M}(1,1) + (v_c - v_{c0})/f_{yc} \cdot \mathbf{M}(1,2) + \mathbf{M}(1,3)}. \end{cases} \tag{15}$$

The 3D reconstruction process is summarized in the flowchart, as shown in Fig. 6. Finally, the complete 3D data can be obtained by stitching the results from each subview.

In addition, it is important to address the color deviation caused by imaging at different viewing angles. We propose a ring light illumination approach to lighten the sample for texture acquisition, which replaces the traditional structured light based on projected illumination for obtaining 2-D texture maps.

D. Denoising Strategy for the Point Cloud Data

The surface of pathological tissues has complex shapes and also different colors. Usually, the following categories of areas are most prone to measurement errors: 1) shadow and dark areas due to the occlusion by complex morphology; 2) mirror-like areas reflect the fringe from the substrate; and 3) highly reflective surface due to the smooth parts or formaldehyde soak. The areas mentioned above will be somehow noisy during the phase map retrieval. We propose a denoising strategy, including three methods to fix the noise problem.

1) Background and Modulation Constraints: The image of the sample being projected by sinusoidal patterns can be expressed as follows:

$$I_n = A(u, v) + B(u, v) \cos\left[\phi(u, v) + \phi'\right] \tag{16}$$

where ϕ is the modulated phase by the sample surface, and ϕ' is a constant phase value for phase shifting.

Areas of low-background light intensity or amplitude mean that no object is present or that the part of the background other than the object is being detected. The noise can be removed by setting appropriate background or amplitude thresholds. It is usually possible to set a small value (e.g., 3 for 8-bit images) for both to filter out invalid point cloud noise from the background. Too large values will cause darker parts of the target to be erroneously filtered out. In this way, two denoising masks can be created by determining whether the background and the modulation are within the preset threshold range.

2) Phase Monotonicity Constraint: When the fringe is reflected from the substrate through the sample surface, this area also has adequate fringe information and cannot be removed by the background intensity and modulation constraints. However, due to the reflection, the phase-shifting direction of the fringe images is opposite to that in the normal area. The phase gradient or the phase monotonicity would be opposite correspondingly. Based on this observation, we can remove this kind of noise by judging the phase gradient, which is defined as follows:

$$d\phi_{r_0} = \frac{\phi(r) - \phi(r - r_0)}{|r_0|}. \tag{17}$$

It is important to note that the smoother target surfaces may have individual derivative sign errors due to inherent noise. Therefore, it is necessary to further synthesize pixels around them to determine whether the sign reversal forms a contiguous domain. This avoids the misidentification of reflective fringes due to random noise. According to the sign of the derivation result, the constraint mask can be generated.

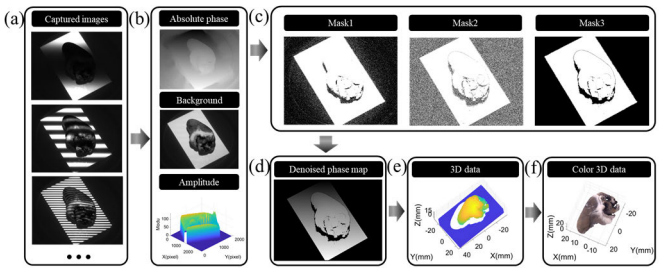

Fig. 7. Overall denoising process of the 3D data. (a) Phase-shifting image captured by the camera. (b) Absolute phase, background, and modulation calculated by phase-shifting algorithm. (c) Three denoising masks using background intensity and modulation constraints, phase monotonicity constraint, and phase jumping constraint. (d) Phase image after denoising. (e) 3D shape. (f) 3D shape with color.

3) Phase Jumping Constraint: Almost noise can be removed by the first two steps; however, the noise near the boundary and highlight region is still challenging. We thereby limit the range of phase jumping between each neighboring pixel pair to detect the noise. Discrete point groups with point numbers exceeding a threshold are connected into the same domain but removed if the point number in a group is less than that. This method also works well in the shaded area and reflection area.

Phase jumps between adjacent pixels imply discontinuity. We divide the entire phase space into a number of contiguous domains based on the magnitude of the difference between neighboring phase values. If neighboring pixels have phase values with deviation less than a certain threshold T_1, they are grouped into a contiguous domain. After grouping all the pixels, the connectivity domains with pixel numbers less than a value T_2 are removed from the final overall phase map, as we do not consider them part of the continuous target. Here, T_1 and T_2 are found based on trying different thresholds and can be used as an empirical value. The criterion is to set the thresholds in such a way that the vast majority of visible recognizable discrete point clouds are removed in multiple experiments with different samples.

The above denoising steps are all performed based on the manipulation of 2-D images, and the overall denoising process is shown in Fig. 7.

E. Evaluation Metrics of the Retrieved 3D Data

The system's measurement accuracy can be reflected by calibration and 3D deviation assessment. First is the calibration accuracy of the camera and projector, which are pinhole modeled, and then, the parameters are calculated using a checkerboard. Eventually, feature points close to the true values are brought into the model, and the reprojection error is calculated by

$$\text{err} = p - \hat{p}(A, T, k, \mathbf{P}). \tag{18}$$

Here, $\mathbf{P}$ is the coordinate of the feature point. A, T, and k are the intrinsic matrix, extrinsic matrix, and distortion parameter of the camera or projector, respectively. The calibration is successful only when the reprojection error has a centrosymmetric distribution with a low standard deviation.

Based on the calibrated camera and projector, we need to perform further 3D measurements on objects with known morphology and compare the results with the real values. Since the point cloud data we acquire is discrete, it needs to be fit to a specific shape. The deviation between the truth and the measured value is then analyzed, and the standard deviation or root-mean-square error (RMSE) is statistically determined. This is how we perform quantitative evaluations of our system.

F. Guidelines Projection for Telemedicine Interaction

Here, we introduce how to project markers as guidelines on specified parts of the sample surface for telemedicine interaction. The whole process is to convert the selected 3D areas of the sample to the DMD coordinates. From (1), we can obtain the relationship between the 3D coordinates $\mathrm{P}_p(X_p, Y_p, Z_p)$ in the projector coordinate system and the image coordinates $\mathrm{p}_\mathrm{p}(u_p, v_p)$ as follows:

$$Z_p \begin{bmatrix} u_p \\ v_p \\ 1 \end{bmatrix} = \begin{bmatrix} f_{x_p} & 0 & u_{p_0} \\ 0 & f_{y_p} & v_{p_0} \\ 0 & 0 & 1 \end{bmatrix} \begin{bmatrix} X_p \\ Y_p \\ Z_p \end{bmatrix}. \tag{19}$$

Since the point cloud data we obtained by (15) is based on the camera coordinate system, we need to convert it to the projector coordinate system through (12). Since the point cloud coordinates are calculated from the image coordinates, the selected 2-D areas or flexible lines in the image coordinates are easily transformed into the 3D areas on the point cloud. Therefore, marking guidelines on the 2-D image is also feasible instead of directly on the point cloud data to project the corresponding marker pattern onto the sample surface.

IV. Results

A. Accuracy Evaluations by Measuring a Standard Plane

We use a piece of ceramic plate to represent a standard plane, which is measured as the sample to evaluate the 3D measurement accuracy of our system. This experiment also determines the optimal coded fringe frequency. We use horizontal fringe patterns with different spatial densities as the coded fringe patterns to retrieve the 3D morphology of the plate. The 3D reconstruction results are shown in Fig. 8. The standard deviation between the reconstructed results and the ideal fit plane is studied to find the optimal fringe density that should be applied in the system.

Refer to camera 1 in Fig. 5. By traversing period values from 6 to 54 pixels, we find the optimal fringe period on the DMD plane is 36 pixels, with a standard deviation of 11.41 μm. We tilt the fringe direction to make it perpendicular to the baseline direction, and the standard deviation goes down from 11.41 to 5.40 μm, as shown in the final result in Fig. 8.

B. Quantitative Evaluations by Measuring a Standard Sphere

We estimate the systematic error by performing 3D measurements on a standard sphere with a nominal radius of 5.00065 mm using horizontal fringe patterns and tilt fringe

Spatial distance unit(pixel)	6	12	18	24	30
Standard error unit(mm)	0.59242	0.71222	0.02197	0.01373	0.01227
Oblique View unit (mm)	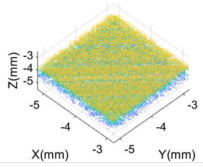	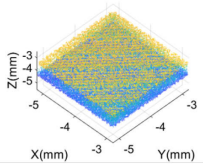	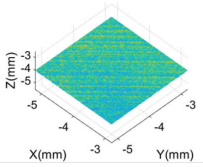	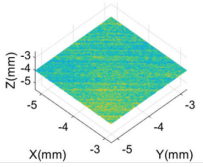	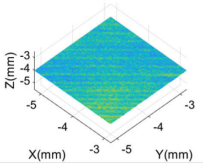
Spatial distance unit(pixel)	36	42	48	54	36 (tilted fringes)
Standard error unit(mm)	0.01141	0.01171	0.01174	0.01207	0.00540
Oblique View unit (mm)	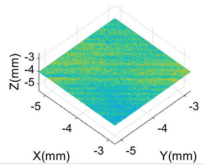	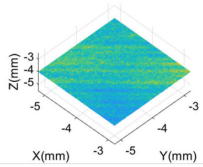	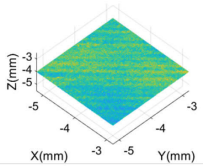	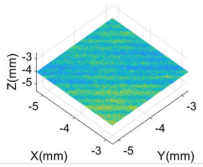	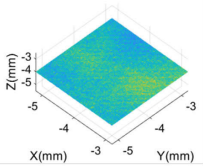

Fig. 8. Standard deviation distribution between the reconstructed and ideal fit planes using fringe patterns with different spatial densities. The first row is the spatial distance between every two strips, representing the fringe period. When the period is minor, errors in the phase unwrapping occur, leading to significant point stratification(periods being 6 and 12). The robustness of the phase unwrapping is better with increasing periods up to 54 pixels. The error is minimized at the fringe period of 36 pixels, implying that using 36 pixels is the optimal frequency. When we switch the fringe direction along the baseline direction, the standard deviation goes down from 11.41 to 5.40 μm.

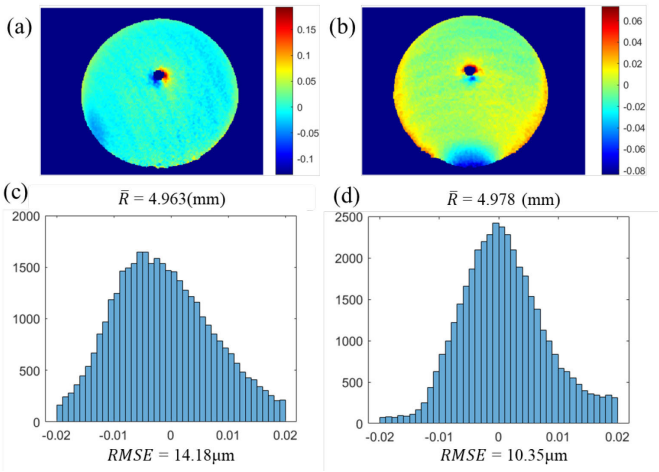

Fig. 9. Comparison of measurement accuracy based on the standard ceramic sphere. (a) Error distributions of the result using horizontal fringe patterns. (b) Error distributions of the result using tilted fringes patterns. (c) Histogram of error using horizontal fringe patterns. (d) Histogram of error using tilted fringe patterns.

patterns, respectively. The measurement result is shown in Fig. 9. The sphere fitting is performed to the 3D data to retrieve the measured radius, and then, the deviation between the result and the fit sphere data is collected. In Fig. 9(a) and (b), we display the deviation distributions, and Fig. 9(c) and (d) shows the corresponding histogram. The radius of the reconstructed spheres using two sets of fringes are 4.963 and 4.978 mm, respectively. Nevertheless, the root means square (rms) goes down from 14.18 to 10.35 μm. Taking 4.978 mm as the retrieved radius, the overall deformation error of the system is 0.45%.

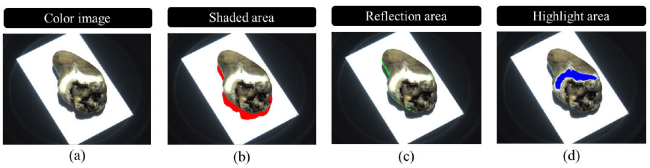

Fig. 10. Noise areas are classified into different types. (a) Sample's color image. (b) Shadow and dark areas due to the occlusion by complex morphology. (c) Light is reflected by the sample surface from the substrate. (d) Highly reflective surface.

C. Denoising of Biological Samples

After verifying the measurement accuracy of the system, we next look at how well the denoising works for point clouds. As shown in Fig. 10, the three colors of red, green, and blue, respectively, represent the shadow areas caused by the complex morphology of the sample surface, reflection areas caused by the reflection of projected light from the substrate surface to the sample surface, and highlight areas caused by smooth parts or formaldehyde soak.

We measured a chicken heart, a throat, and a gizzard to test the robustness of the denoising method used on different biological samples. The results are shown in Fig. 11. The 3D data of the biological samples before denoising is shown in Fig. 11(a1)–(a3), from which we can see that many flying spots are far from the object's actual position. The 3D data after denoising is shown in Fig. 11(b1)–(b3), from which we can find that our method can effectively eliminate the unmeasurable part or the additionally introduced error while retaining the information of the object itself. The color information is obtained directly from the color camera under white LED illumination. The 3D data with color information

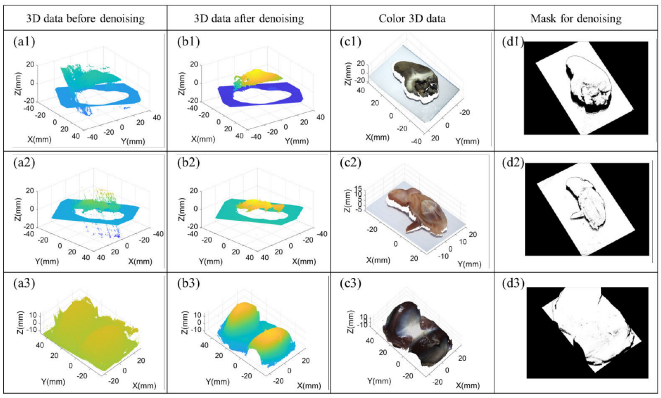

Fig. 11. Comparison of the effect before and after denoising. (a1)–(a3) Before denoising. (b1)–(b3) After denoising. (c1)–(c3) Result of coloring after denoising. (d1)–(d3) Masks generated during the denoising process.

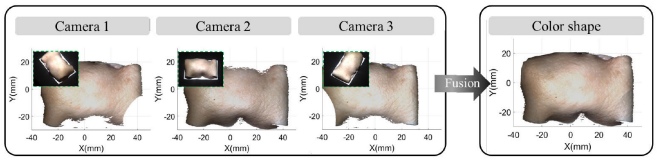

Fig. 12. Cloud registration with data stitching and color fusion, the green box is the 2-D images captured by each camera in the three subviews, respectively.

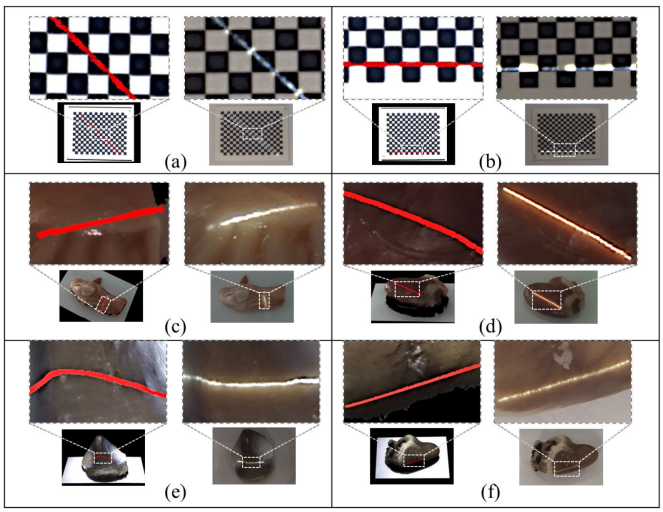

Fig. 13. Experimental result of interactive guidelines projection. (a) and (b) Position of the line on the 3D data (left) and the position of the projected guidelines on the calibration board (right). (c)–(f) Position of the line on the 3D data (left) and the position of the projected guidelines on the biological samples (right).

are shown in Fig. 11(c1)–(c3). The mask generated by the denoising method is also provided Fig. 11(d1)–(d3).

After the 3D data from each viewpoint is denoised, data stitching and color fusion are performed to obtain a complete 3D result of the sample. As shown in Fig. 12, the left side is the point cloud data acquired from each camera view, and the right side is the final integrated color 3D data.

D. Experiments of Interactive Guidelines Projection

To test the functionality and accuracy of our system in the inverse projection of interactive guidelines, we conducted projection experiments on the calibration board for accuracy verification and four biological samples to observe actual application effects. The results are shown in Fig. 13. The left side of Fig. 13(a) and (b) shows the 3D reconstruction result of the calibration board, and the red lines are manually drawn on the 3D surface. The right side is the projected guidelines on the samples. The linewidth and color can be adjusted according to environmental requirements.

By comparing the position of the lines on the 3D data with the position of the projected guidelines on the samples, we can conclude that our projection accuracy is guaranteed. On this basis, we have done the same experiments on complex biological tissue samples. The results of the experiment are shown in Fig. 13(c)–(f). In order to photograph the projected thin lines more clearly, we reduced the brightness of the ambient lighting. Overall, the experimental results show the effectiveness of our proposed system and methodology in providing technical support for telemedicine through interactive guidelines projection.

V. Discussion

A. Calibration Patterns Comparison: Checkerboard Versus Circular Pattern

Common calibration patterns can be generally categorized into a checkerboard and circular pattern. The black and white intersections of the checkerboard pattern are used as corner points. Circular patterns, on the other hand, extract circle centers as corner points. The checkerboard pattern provides sufficiently accurate results when calibrating a camera, but the situation is different when calibrating the projector. It is impossible to extract accurate phase values at the black–white junction because the phase here is wildly inaccurate due to out-of-focus effects and luminance diffusion. It is necessary to choose an area with a white background to extract the phase. White circular patterns can accomplish this. However, if perspective distortion exists, there will be center positioning errors when circular markers are used. As shown in Fig. 4(a)–(c), the circular markers become ellipses after perspective distortion, so the center extracted using the circle center extraction algorithm deviates from the original center. The board should be arranged in tilted enough poses, which aggravates the perspective distortion. Our proposed method eliminates the side effect of perspective distortion and is quite flexible to realize.

B. Optimal Design of Fringe Pattern Sequence

When we design the pattern sequence, we mainly consider the following aspects. First, the influence of random error on 3D measurement can be effectively reduced by increasing the phase-shifting steps as well as the fringe frequency. However, too many phase-shifting steps will affect the measurement speed, and the fringe frequency is not the higher, the better. Since the optical transfer function of the projected light path is not ideal, the phenomenon of out-of-focus will occur. This is why we traverse multiple fringe frequencies for the accuracy evaluation experiments on the 3D measurements of the plane. In addition, a reasonable sequence of fringe frequencies and phase-shifting steps are also crucial factors affecting

measurement efficiency. For example, the fringe frequency sequence 1-10-100 is better than 1-50-100 because the latter is prone to cause errors in phase unwrapping. The fringe frequency sequence 1-8-64 is better than 1-2-4-8-16-32-64 because the latter requires many more frames to obtain the complete unwrapped phase. In our system, we tried to use a geometric frequency sequence as much as possible and give more phase-shifting steps to the highest frequency fringe while guaranteeing acceptable measurement speed and errors for the practical application.

C. Influence of Tilted Fringes on Measurement Accuracy

One thing to remember when we design the fringe direction for structured light 3D measurement is to correlate the fringe bending degree with the variance in height or depth. Imagine that if we project fringes with its direction along the baseline, a change in the object's height causes the fringe to shift along the ridge rather than being bent; therefore, the shape cannot be reflected by the fringe changing. On the contrary, the best design is to have the change in height cause the fringes to bend in the direction perpendicular to the ridge. Therefore, we improve the accuracy of our system by setting the fringe direction in three different directions considering each camera position. However, the tilted fringe has a jagged effect in practice due to the digitized discrete projector pixels. In order to eliminate the jaggedness, we slightly defocus the projector lens, which ensures sufficient fringe contrast and eliminates the jaggedness through the defocused low-pass filter effect.

D. Threshold Setting for 3D Denoising Process

Much of our basis in data denoising comes from the intermediate variables during the process. They have a precise physical meaning and can guide us in filtering out invalid points. The background calculated in the phase-shifting process represents the intensity distribution of the target surface and can be used to extract a valid target area to reduce the amount of computation. At the same time, the modulation calculated in the phase-shifting process reflects the contrast of the fringe and indicates the reliability of the phase-shifting accuracy. Usually, the background and modulation are somewhat related. So, to avoid the dark target region being removed undesirably by setting a uniform threshold, different thresholds need to be set in areas with different brightness to determine the effective region.

E. Realization of Rapid Measurement and Inverse Projection

The digitized projection module consists of an optical machine and a controller. The controller in our system is used in two ways: one as a second screen to project a specific pattern and the other to preload a sequence of coded fringe patterns into its memory. Both modes have advantages and disadvantages and that are used to fulfill different divisions of the system functions. The preloaded mode has a long preparation time but projects very fast. Furthermore, the measurement efficiency can be maximized by synchronizing the exposure signal with the cameras. The second-screen mode can be used to project a flexible marker pattern inversely, but its speed just manages to be without noticeable delay. Therefore, the combination and flexible switching of the two methods can satisfy both the fast measurement requirements and the flexible inverse projection function of interactive guidelines. For our system, 3D reconstruction can be performed in less than 3 s, including data acquisition and processing.

VI. Conclusion

In this article, we presented a structured light 3D measuring system that realizes color 3D observation of pathological tissue samples and provides a potential way for the remote expert to provide cutting guidance of the pathological sample interactively. Based on the layout between the three cameras and the projector, we propose a high-precision 3D reconstruction for each subsystem using sinusoidal structured patterns with the phase gradient direction in line with each baseline direction. The measurement accuracy is experimentally improved compared with three cameras sharing the same phase-shifted fringes.

For system calibration, our proposed method using the diagonal center of the white squares on the checkboard as feature points successfully avoids the side effect of perspective distortion on center positioning. For the noise during the 3D imaging process, we proposed a denoising strategy for the point cloud data of tissues based on background and modulation constraints, phase monotonicity check, and phase jumping compensation, respectively.

By flexibly switching the working modes of the projector and synchronizing the exposure with the cameras, our system can complete a 3D reconstruction in less than 3 s. The accuracy evaluation experiments on the standard plane and sphere show that our system achieves 3D results with a repeatability error of less than 10 μm at a field of view of 6 $\times$ 10 cm.

Finally, the interactive guideline projection method is experimentally validated, meeting the requirements for resection imaging of ex vivo specimens and demonstrating the potential application in pathology telemedicine assistance.

References

[1] Y. Cao et al., "Multiparameter synchronous measurement with IVUS images for intelligently diagnosing coronary cardiac disease," *IEEE Trans. Instrum. Meas.*, vol. 70, pp. 1–10, 2021, doi: 10.1109/TIM.2020.3036067.

[2] X. Li, W. Li, and R. Tao, "Staged detection–identification framework for cell nuclei in histopathology images," *IEEE Trans. Instrum. Meas.*, vol. 69, no. 1, pp. 183–193, Jan. 2020, doi: 10.1109/TIM.2019.2894044.

[3] N. M. Hjelm, "Benefits and drawbacks of telemedicine," *J. Telemedicine Telecare*, vol. 11, no. 2, pp. 60–70, Mar. 2005, doi: 10.1258/1357633053499886.

[4] J. Craig and V. Patterson, "Introduction to the practice of telemedicine," *J. Telemedicine Telecare*, vol. 11, no. 1, pp. 3–9, Jan. 2005.

[5] C. De Capua, A. Meduri, and R. Morello, "A smart ECG measurement system based on web-service-oriented architecture for telemedicine applications," *IEEE Trans. Instrum. Meas.*, vol. 59, no. 10, pp. 2530–2538, Oct. 2010, doi: 10.1109/TIM.2010.2057652.

[6] S. G. Mougiakakou, I. K. Valavanis, N. A. Mouravliansky, K. S. Nikita, and A. Nikita, "DIAGNOSIS: A telematics-enabled system for medical image archiving, management, and diagnosis assistance," *IEEE Trans. Instrum. Meas.*, vol. 58, no. 7, pp. 2113–2120, Jul. 2009, doi: 10.1109/tim.2009.2015538.

[7] J. Xu and S. Zhang, "Status, challenges, and future perspectives of fringe projection profilometry," *Opt. Lasers Eng.*, vol. 135, Dec. 2020, Art. no. 106193, doi: 10.1016/j.optlaseng.2020.106193.

[8] K. Fu, Y. Xie, H. Jing, and J. Zhu, "Fast spatial–temporal stereo matching for 3D face reconstruction under speckle pattern projection," *Image Vis. Comput.*, vol. 85, pp. 36–45, May 2019, doi: 10.1016/j.imavis.2019.02.007.

[9] P. Zhou, J. Zhu, W. Xiong, and J. Zhang, "3D face imaging with the spatial–temporal correlation method using a rotary speckle projector," *Appl. Opt.*, vol. 60, no. 20, p. 5925, Jul. 2021, doi: 10.1364/ao.430101.

[10] L. Shao, P. Kner, E. H. Rego, and M. G. L. Gustafsson, "Super-resolution 3D microscopy of live whole cells using structured illumination," *Nature Methods*, vol. 8, no. 12, pp. 1044–1046, Dec. 2011, doi: 10.1038/nmeth.1734.

[11] Y. Hu, Q. Chen, S. Feng, and C. Zuo, "Microscopic fringe projection profilometry: A review," *Opt. Lasers Eng.*, vol. 135, Dec. 2020, Art. no. 106192, doi: 10.1016/j.optlaseng.2020.106192.

[12] Y. Li, J. Qian, S. Feng, Q. Chen, and C. Zuo, "Deep-learning-enabled dual-frequency composite fringe projection profilometry for single-shot absolute 3D shape measurement," *Opto-Electron. Adv.*, vol. 5, no. 5, p. 210021, 2022, doi: 10.29026/oea.2022.210021.

[13] Z. Wu et al., "Three-dimensional nanoscale reduced-angle ptychotomographic imaging with deep learning (RAPID)," *eLight*, vol. 3, no. 1, p. 7, Apr. 2023, doi: 10.1186/s43593-022-00037-9.

[14] C. Liu, Z. Jiang, X. Wang, Y. Zheng, Y.-W. Zheng, and Q.-H. Wang, "Continuous optical zoom microscope with extended depth of field and 3D reconstruction," *PhotoniX*, vol. 3, no. 1, p. 20, Sep. 2022, doi: 10.1186/s43074-022-00066-0.

[15] J. Han, L. Shao, D. Xu, and J. Shotton, "Enhanced computer vision with Microsoft Kinect sensor: A review," *IEEE Trans. Cybern.*, vol. 43, no. 5, pp. 1318–1334, Oct. 2013, doi: 10.1109/TCYB.2013.2265378.

[16] S. Bi, C. Yuan, C. Liu, J. Cheng, W. Wang, and Y. Cai, "A survey of low-cost 3D laser scanning technology," *Appl. Sci.*, vol. 11, no. 9, p. 3938, Apr. 2021, doi: 10.3390/app11093938.

[17] C. Zuo, S. Feng, L. Huang, T. Tao, W. Yin, and Q. Chen, "Phase shifting algorithms for fringe projection profilometry: A review," *Opt. Lasers Eng.*, vol. 109, pp. 23–59, Oct. 2018, doi: 10.1016/j.optlaseng.2018.04.019.

[18] G. Wu, T. Yang, F. Liu, and K. Qian, "Suppressing motion-induced phase error by using equal-step phase-shifting algorithms in fringe projection profilometry," *Opt. Exp.*, vol. 30, no. 11, p. 17980, May 2022, doi: 10.1364/oe.459087.

[19] C. Chen, H. Wang, Z. Zhang, and F. Gao, "Three-dimensional reconstruction from a fringe projection system through a planar transparent medium," *Opt. Exp.*, vol. 30, no. 19, p. 34824, Sep. 2022, doi: 10.1364/oe.471265.

[20] X. Bai, N. Gao, Z. Zhang, and D. Zhang, "Person recognition using 3-D palmprint data based on full-field sinusoidal fringe projection," *IEEE Trans. Instrum. Meas.*, vol. 68, no. 9, pp. 3287–3298, Sep. 2019, doi: 10.1109/TIM.2018.2877226.

[21] Y. Hu, Q. Chen, S. Feng, T. Tao, A. Asundi, and C. Zuo, "A new microscopic telecentric stereo vision system–calibration, rectification, and three-dimensional reconstruction," *Opt. Lasers Eng.*, vol. 113, pp. 14–22, Feb. 2019, doi: 10.1016/j.optlaseng.2018.09.011.

[22] Q. Zhang and X. Su, "High-speed optical measurement for the drumhead vibration," *Opt. Exp.*, vol. 13, no. 8, p. 3110, Apr. 2005, doi: 10.1364/opex.13.003110.

[23] B. Li and S. Zhang, "Flexible calibration method for microscopic structured light system using telecentric lens," *Opt. Exp.*, vol. 23, no. 20, p. 25795, Oct. 2015, doi: 10.1364/oe.23.025795.

[24] P. Hu, S. Yang, H. Deng, X. Qu, and G. Zhang, "Accurate 3-D shape measurement for large objects using speckle-assisted fringe projection and global markers localization," *IEEE Trans. Instrum. Meas.*, vol. 71, pp. 1–10, 2022, doi: 10.1109/TIM.2022.3181931.

[25] T. Cheng, X. Liu, L. Qin, M. Lu, C. Xiao, and S. Li, "A practical micro fringe projection profilometry for 3-D automated optical inspection," *IEEE Trans. Instrum. Meas.*, vol. 71, pp. 1–13, 2022, doi: 10.1109/TIM.2022.3196738.

[26] M. Wang, Y. Yin, D. Deng, X. Meng, X. Liu, and X. Peng, "Improved performance of multi-view fringe projection 3D microscopy," *Opt. Exp.*, vol. 25, no. 16, p. 19408, Aug. 2017, doi: 10.1364/oe.25.019408.

[27] J. Qian, T. Tao, S. Feng, Q. Chen, and C. Zuo, "Motion-artifact-free dynamic 3D shape measurement with hybrid Fourier-transform phase-shifting profilometry," *Opt. Exp.*, vol. 27, no. 3, p. 2713, Feb. 2019, doi: 10.1364/oe.27.002713.

[28] B. Zhang, S. Lin, J. Lin, and K. Jiang, "Single-shot high-precision 3D reconstruction with color fringe projection profilometry based BP neural network," *Opt. Commun.*, vol. 517, Aug. 2022, Art. no. 128323, doi: 10.1016/j.optcom.2022.128323.

[29] Z. Zhang, C. E. Towers, and D. P. Towers, "Time efficient color fringe projection system for 3D shape and color using optimum 3-frequency selection," *Opt. Exp.*, vol. 14, no. 14, p. 6444, 2006, doi: 10.1364/oe.14.006444.

[30] W. Yin et al., "Single-shot 3D shape measurement using an end-to-end stereo matching network for speckle projection profilometry," *Opt. Exp.*, vol. 29, no. 9, p. 13388, Apr. 2021, doi: 10.1364/oe.418881.

[31] Z. H. Zhang, "Review of single-shot 3D shape measurement by phase calculation-based fringe projection techniques," *Opt. Lasers Eng.*, vol. 50, no. 8, pp. 1097–1106, Aug. 2012, doi: 10.1016/j.optlaseng.2012.01.007.

[32] K. Chen, J. Xi, Y. Yu, S. Tong, and Q. Guo, "Three-dimensional measurement of object surfaces with complex shape and color distribution based on projection of color fringe patterns," *Appl. Opt.*, vol. 52, no. 30, p. 7360, Oct. 2013, doi: 10.1364/ao.52.007360.

[33] C. Zuo, L. Huang, M. Zhang, Q. Chen, and A. Asundi, "Temporal phase unwrapping algorithms for fringe projection profilometry: A comparative review," *Opt. Lasers Eng.*, vol. 85, pp. 84–103, Oct. 2016, doi: 10.1016/j.optlaseng.2016.04.022.

[34] H. Zhao, C. Zhang, C. Zhou, K. Jiang, and M. Fang, "Circular fringe projection profilometry," *Opt. Lett.*, vol. 41, no. 21, p. 4951, Nov. 2016, doi: 10.1364/ol.41.004951.

[35] M. Ratnam, M. Saxena, and S. S. Gorthi, "Circular fringe projection technique for out-of-plane deformation measurements," *Opt. Lasers Eng.*, vol. 121, pp. 369–376, Oct. 2019, doi: 10.1016/j.optlaseng.2019.05.004.

[36] F. Lu and C. Wu, "Three-dimensional measurement of object surface by using ellipse binary defocusing projection," *J. Eur. Opt. Soc.-Rapid Publications*, vol. 13, no. 1, p. 29, Dec. 2017, doi: 10.1186/s41476-017-0055-.

Yan Hu received the Bachelor of Science degree from the Wuhan University of Technology, Wuhan, China, in 2013, and the Ph.D. degree in optical engineering from the Nanjing University of Science and Technology, Nanjing, China, in 2019.

He is currently an Associate Professor with the School of Electronic and Optical Engineering, Nanjing University of Science and Technology. His research interests include 3D sensing, computational optoelectronic imaging, and image processing.

Dr. Hu received the Young Optical Science and Technology Award from the Jiangsu Optical Society in 2022.

Zhongwei Liang received the bachelor's degree in applied physics from the Tianjin University of Technology, Tianjin, China, in 2020. He is currently pursuing the master's degree in optical engineering with the Nanjing University of Science and Technology, Nanjing, China.

His research interests include 3D measurement using structured light and computer vision.

Kehui Wang received the bachelor's degree in computer and science from the Department of Computer and Science, Ludong University, Yantai, China, in 2005, and the master's degree in computer applied technology from Harbin Engineering University, Harbin, China, in 2008.

His research interests include software engineering, medical image analysis, and embedded systems of medical instruments.

Kun Gui received the bachelor's degree in computer and science from the Department of Computer and Science, Harbin Engineering University, Harbin, China, in 2007, and the master's degree in computer applied technology from Harbin Engineering University, in 2010.

His research interests include medical image analysis, big data analysis, and deep learning techniques.

Jin Zhang received the Bachelor of Medicine degree in medical examination from the College of Medical Laboratory, Dalian Medical University, Dalian, China, in 2006.

His research interests include pathological techniques and pathological big data analysis.

Qian Chen received the B.Sc. and Ph.D. degrees from the School of Electronic and Optical Engineering, Nanjing University of Science and Technology, Nanjing, China, in 1987 and 1996, respectively.

He is currently a Chang Jiang Scholar and a Professor with the School of Electronic and Optical Engineering, Nanjing University of Science and Technology. He has authored two books in the areas of imaging and signal processing. His research interests include night vision technology, photoelectric device and image processing, computational imaging, and 3D sensing.

Prof. Chen was awarded the Second Prize of National Technical Invention in 2018, the Second Prize of National Science and Technology Progress in 2008, and the First Prize of Science and Technology of Jiangsu Province in 2020. He received the National Innovation Award in 2020.

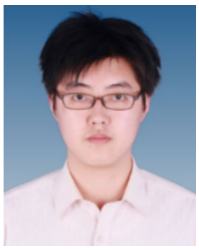

Chao Zuo (Senior Member, IEEE) received the B.Sc. and Ph.D. degrees from the School of Electronic and Optical Engineering, Nanjing University of Science and Technology (NJUST), Nanjing, China, in 2009 and 2014, respectively.

He is currently a Professor with the Department of Electronic and Optical Engineering, NJUST, where he is also the Group Leader of the Smart Computational Imaging Laboratory. His research interests include computational imaging and optical information processing technology.

Prof. Zuo has been selected into the Natural Science Foundation of China (NSFC) for Excellent Young Scholars and Outstanding Youth Foundation of Jiangsu Province.